PRINTING TECHNOLOGY

Ultrathin high-resolution flexographic printing using nanoporous stamps

Sanha Kim,[1] Hossein Sojoudi,[1,2] Hangbo Zhao,[1] Dhanushkodi Mariappan,[1] Gareth H. McKinley,[1] Karen K. Gleason,[2] A. John Hart[1]*

Since its invention in ancient times, relief printing, commonly called flexography, has been used to mass-produce artifacts ranging from decorative graphics to printed media. Now, higher-resolution flexography is essential to manufacturing low-cost, large-area printed electronics. However, because of contact-mediated liquid instabilities and spreading, the resolution of flexographic printing using elastomeric stamps is limited to tens of micrometers. We introduce engineered nanoporous microstructures, comprising polymer-coated aligned carbon nanotubes (CNTs), as a next-generation stamp material. We design and engineer the highly porous microstructures to be wetted by colloidal inks and to transfer a thin layer to a target substrate upon brief contact. We demonstrate printing of diverse micrometer-scale patterns of a variety of functional nanoparticle inks, including Ag, ZnO, WO_3, and CdSe/ZnS, onto both rigid and compliant substrates. The printed patterns have highly uniform nanoscale thickness (5 to 50 nm) and match the stamp features with high fidelity (edge roughness, ~0.2 μm). We derive conditions for uniform printing based on nanoscale contact mechanics, characterize printed Ag lines and transparent conductors, and achieve continuous printing at a speed of 0.2 m/s. The latter represents a combination of resolution and throughput that far surpasses industrial printing technologies.

INTRODUCTION

For centuries, innovations in printing technologies have gone hand-in-hand with advances in communication, education, and industrialization. Relief printing, which was invented in China using hand-carved woodblock stamps in ~200 CE (*1*), involves loading of ink onto raised stamp structures, followed by transfer to the target substrate by mechanical contact. The invention of metal relief printing stamps in the year ~1230 enabled mass production of books (*2*), and the invention of rubber stamps in the 1860s enabled roll-to-roll production of high-quality graphics (*3*). This latter process is commonly called flexography.

Further breakthroughs in printing technologies are now essential to scalable manufacturing of electronic devices (*4*, *5*) in large-area and unconventional formats, such as on windows, contact lenses, ultrathin membranes, and flexible films. Low-cost printed electronics are also central to the vision of an "internet of things," encompassing ubiquitous connected devices and means of tracking everyday objects, including medicines, foods, and products during transportation and use (*6*). However, the inability to print electronic materials with micrometer-scale resolution (that is, minimum feature size of 1 to 10 μm) at high throughput is a major roadblock in this pursuit (*7*–*9*). For example, thin-film transistors with smaller lateral dimensions have higher bandwidth and on/off switching speed along with reduced parasitic capacitance, operation voltage, and power consumption. Narrower and thinner conductive lines are also essential to realize metal grid electrodes with improved transparency, and high-resolution displays having micrometer-scale transistor backplane features.

In addition to flexography (*10*, *11*), the mainstream methods for printing electronic materials include inkjet (*12*–*14*), screen (*15*–*18*), and gravure (intaglio) (*19*–*22*) printing. The suitability of each method for a particular application is determined by its resolution, throughput, and materials compatibility, among other attributes. For example, inkjet printing is compatible with many colloidal and polymer inks, yet the size of the droplet that can be ejected from the nozzle aperture is, at present, no less than 10 to 20 μm (*23*). Flexography is also compatible with a wide variety of substrates and inks, but its resolution is limited to 50 to 100 μm (*7*–*11*) despite the capability to manufacture rubber stamps with micrometer and submicrometer feature sizes (*24*). For high-quality flexographic printing, the liquid films need to be thin enough to avoid spreading out from the contact area when compressed, yet such thin films tend to dewet from the stamp surface due to hydrodynamic instability. Higher-resolution printing technologies have been invented and demonstrated, including microcontact (*25*), nanotransfer (*26*), electrohydrodynamic (*27*), and dip-pen (*28*, *29*) methods, yet these lack the throughput and versatility of the mainstream methods.

To enable the next generation of relief printing for electronics manufacturing, we conceived a microstructured nanoporous stamp material that enables ultrathin, high-resolution direct printing of colloidal inks. The stamp is fabricated using patterned aligned carbon nanotubes (CNTs) conformally coated with a thin polymer, such that its porosity, mechanical properties, and surface chemistry enable capillary-driven loading of ink and nanoscale contact-mediated ink transfer. We show that diverse patterns of a variety of electronic nanomaterials, including Ag, ZnO, WO_3 nanoparticles (NPs), and CdSe/ZnS quantum dots (QDs), can be directly printed with micrometer-scale resolution and that the process can be scaled to industrially relevant throughput.

RESULTS

Engineering CNT microstructures as a nanoporous stamp

In Figure 1A we show a schematic description of the printing process using nanoporous stamps, along with exemplary printed materials. First, the polymer-CNT stamp is loaded with an NP-based ink via immersion or spin coating, causing the ink to be drawn into the nanoscale pores within each microstructure (fig. S1) by capillary wicking.

[1]Department of Mechanical Engineering, Massachusetts Institute of Technology, Cambridge, MA 02139, USA. [2]Department of Chemical Engineering, Massachusetts Institute of Technology, Cambridge, MA 02139, USA.
*Corresponding author. Email: ajhart@mit.edu

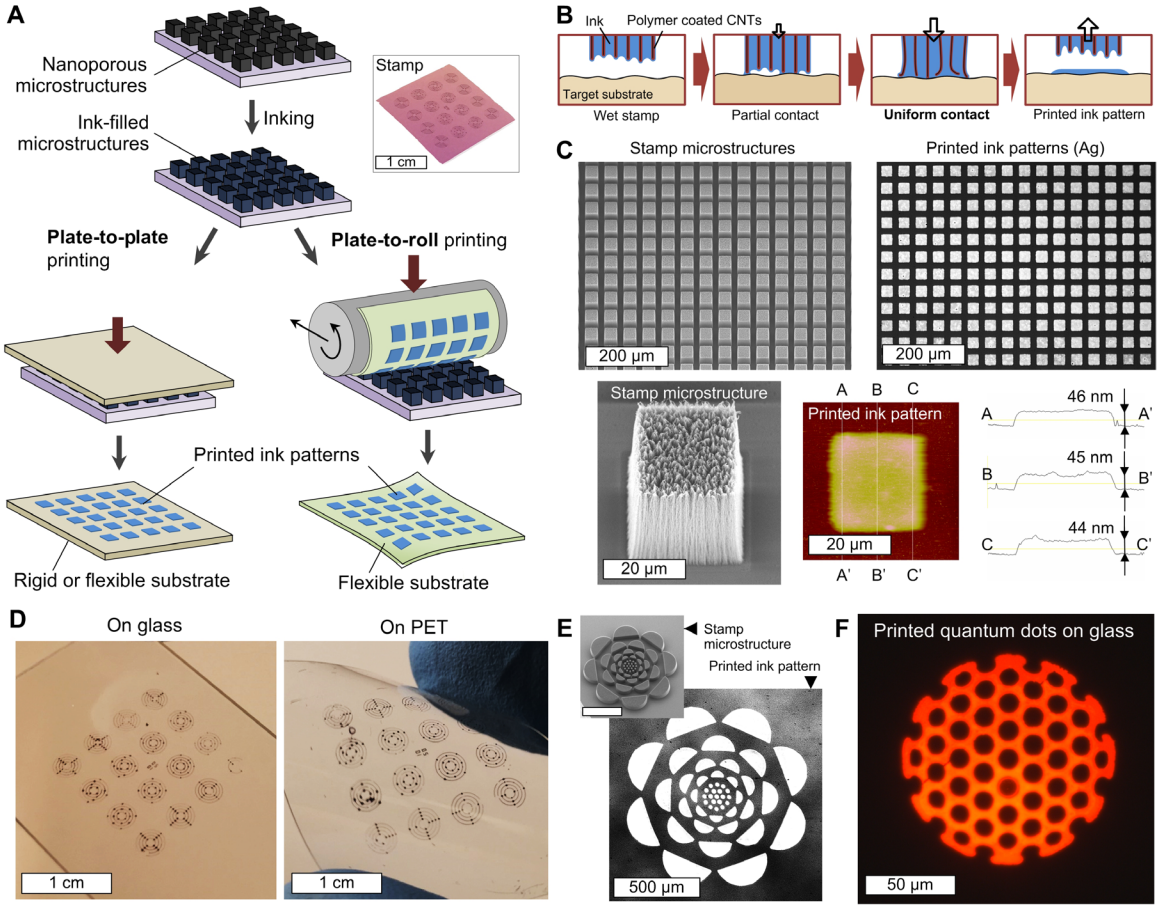

Fig. 1. Direct printing of ultrathin colloidal ink patterns using microstructured nanoporous stamps. Schematics of the printing procedure (**A**) and the uniform transfer of ink (**B**) from the nanoporous stamp to the target substrate surface via conformal contact. (**C**) Scanning electrode microscopy (SEM) images of stamp features comprising an array of squares (side length, 25 µm), along with corresponding optical and atomic force microscopy (AFM) images of the resulting printed Ag ink [particle size, <10 nm; 50 to 60 weight % (wt %) in tetradecane] patterns. (**D**) Photographs of printed Ag ink patterns on a rigid glass plate and on a flexible polyethylene terephthalate (PET) film. (**E**) SEM image of the stamp feature (upper left) and optical microscope image of the printed Ag NP ink pattern (lower right) of a flower-like pattern with feature widths varying from 20 to 150 µm. (**F**) Fluorescence microscope image (wavelength emission, 620 nm) of printed QD ink (CdSe/ZnS, ~5 to 6 nm, 10 wt % dispersed in tetradecane) of a pattern with minimum internal linewidth of 5 µm and hole size of 11 µm.

Next, the stamp is brought into contact with a target substrate. This causes transfer of a thin ink layer that matches the pattern of the microstructures on the stamp with high fidelity (Fig. 1B). For example, square patterns (side length, 25 µm; spacing, 10 µm) of Ag ink (particle size, <10 nm; see Materials and Methods) printed using the nanoporous stamp have a corner radius of 3 µm, an edge roughness of 0.2 µm, and a uniform thickness of ~45 nm (Fig. 1C). As discussed here, we have demonstrated ultrathin flexographic printing of a variety of functional inks on both rigid and flexible substrates (Fig. 1, D to F) and shown its scalability to high rates (>0.1 m/s) without loss of fidelity.

To design the nanoporous stamp material, we considered three key requirements: (i) the stamp must have pores larger than the colloidal ink particles yet significantly smaller than the features to be printed, (ii) the porous stamp must allow infiltration of the ink solvent yet resist deformation due to capillary forces, and (iii) the stamp must be mechanically compliant yet durable, enabling uniform contact with the target substrate without buckling or yielding of the microscale features of the stamp.

To fabricate the stamp (Fig. 2A), first vertically aligned CNT arrays (CNT "forests") are grown on lithographically patterned silicon substrates by atmospheric pressure chemical vapor deposition (CVD). The cross-sectional shape of the stamp features is determined by the CNT growth catalyst pattern (fig. S2); therefore, within the dimensional limits of the photolithography and CNT forest growth processes, any desired pattern can be fabricated (*30*, *31*). As a structure, the CNT arrays are highly porous (~99% porosity) (*32*, *33*) and mechanically compliant (compressive modulus typically 5 to 100 MPa) (*34*). The mechanical behavior of CNT arrays is similar to that of open-cell foams when compressed to moderate strains, and their modulus can be tuned over a wide range by the diameter, density, and connectivity of the CNTs (*35*, *36*).

However, the top surface of the as-grown CNT microstructures comprises clusters of tangled CNTs (fig. S3), arising from the CNT self-organization process (*33*, *37*). When the hydrocarbon source is introduced to the reactor, the CNTs first grow in random directions until a critical density for vertically aligned growth is reached (*38*). As

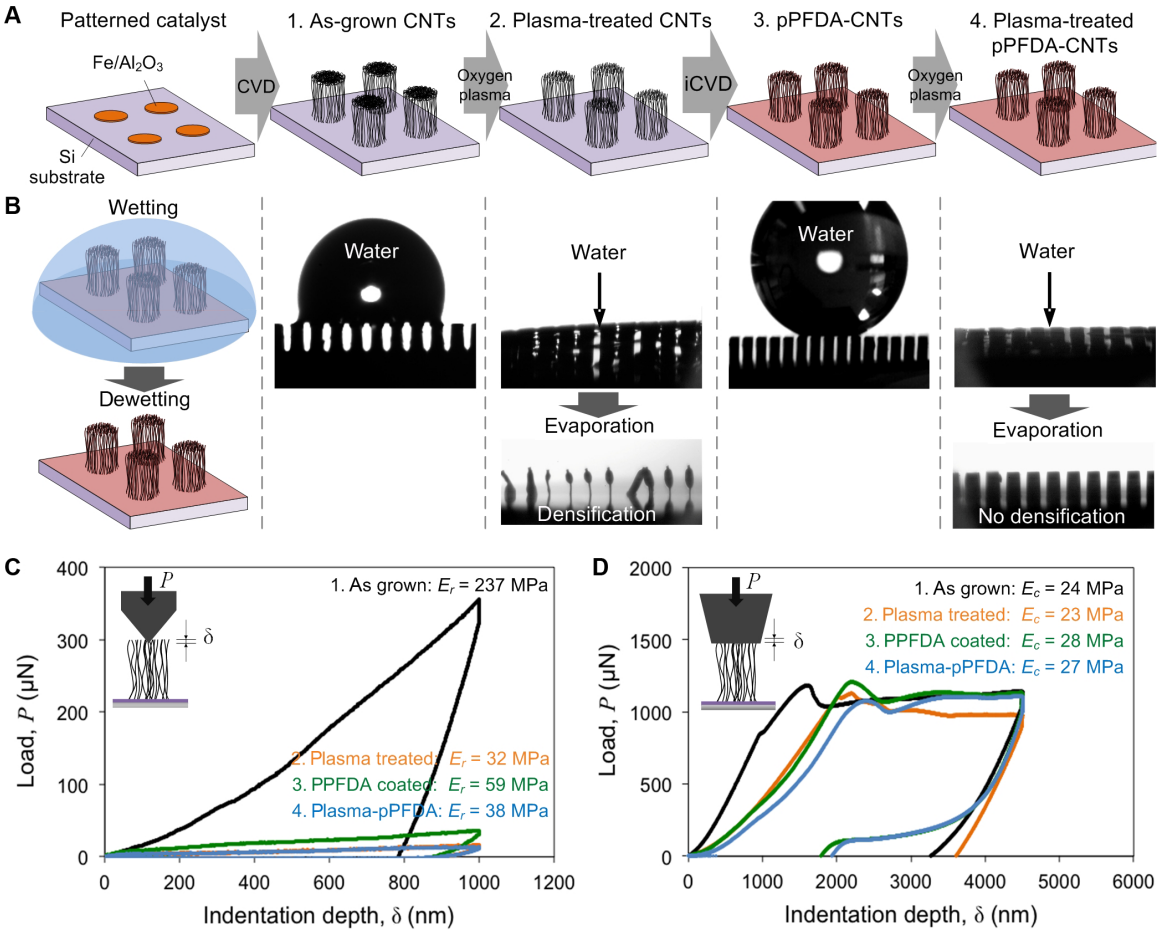

Fig. 2. Fabrication, wetting behavior, and mechanical properties of microstructured nanoporous stamps. (**A**) Schematic of the stamp fabrication process. (**B**) Optical images of the wetting/dewetting behavior after each step (~10 μl of water droplet). Load-displacement curves obtained using a 1-μm radius conical tip (**C**) and a flat tip (**D**), respectively, to measure the surface modulus and the overall elastic modulus in compression.

a result, a tangled "crust" layer (thickness, <1 μm) is carried at the top of the forest and enforces the individual CNTs that have different diameters and growth rates to grow vertically as a monolith (*37*). However, the stiff and rough crust is not desirable for high-resolution printing because it results in nonuniform contact against the target substrate. Indentation tests with a sharp (10-μm conical) tip and compression tests with a flat tip (Fig. 2, C and D), respectively, reveal that the surface modulus (~240 MPa) of as-grown CNT arrays is much greater than the compressive modulus (~24 MPa). The surface modulus is the reduced Young's modulus determined from the localized load-displacement behavior near the surface (*39*), and the compressive modulus is defined from uniaxial compression along the CNT alignment direction. After brief oxygen plasma etching, which removes the crust (fig. S4), the surface modulus (~32 MPa) is comparable to the compressive modulus. The surface compliance enables the CNTs to conformally contact the target substrate during printing. Also, the CNT microstructure matches the dimensions of the catalyst pattern, yet the plasma treatment etches both the top and sidewalls of the CNT microstructures, slightly narrowing their width (fig. S5). Therefore, this reduction must be considered when designing the CNT growth patterns to achieve a target printed feature size.

The surface chemistry of the CNTs must also be engineered to enable infiltration of the ink and to prevent elastocapillary densification of the CNT microstructures (Fig. 2B). CNT forests are typically hydrophobic (*40*), but oxygen plasma etching creates surface defects and promotes attachment of oxygen-containing surface groups, rendering the CNT forest hydrophilic (*41*). As a result, upon liquid infiltration, the CNT microstructures may shrink slightly, and during liquid evaporation, the capillary force exerted by the contracting meniscus can overcome the elastic restoring forces of the deformed CNTs, causing significant densification and mechanical damage (video S1) (*42*). Notably, elastocapillary densification upon recession of solvent has been used to densify and shape CNT forests and other nanostructures into a variety of complex architectures (*43*, *44*). However, this is not desirable for stamp fabrication and repeated printing operations.

To prevent capillary-induced deformation of the CNT microstructures while retaining their porosity, we coat the CNTs with a thin layer (~20 nm) of poly-perfluorodecylacrylate (pPFDA) using initiated CVD (iCVD) (*45*). The PFDA monomer diffuses into the porous CNT microstructures in the vapor phase and results in a conformal coating of the CNTs (fig. S3). The iCVD polymer coating is followed by a second oxygen plasma treatment to remove any pPFDA deposited in a nonconformal manner as a result of condensation of the monomer at the tip of the CNT forest. The pPFDA-coated CNT microstructures do not shrink or collapse upon liquid infiltration

and solvent evaporation (video S2 and fig. S6). The second plasma treatment step is key to enable infiltration of ink for printing (video S3 and fig. S7). The surface modulus and uniaxial compressive modulus of the coated CNT microstructures are 38 and 27 MPa, respectively, corresponding to a 10 to 20% increase due to the polymer coating. We expect the resistance to elastocapillary densification is due to the reinforcement of individual CNTs by the pPFDA coating and development of pPFDA nanowelds at CNT-CNT contact points. Together, these reinforcements increase the lateral rigidity of the CNT forest, which has been found to be essential to prevent shrinkage upon evaporation (*42*). The pPFDA coating and the subsequent plasma treatment also certainly change the internal surface area per unit volume of the forests and the adhesion between CNTs and CNT bundles; the influence of these effects on the mechanics and stability of the CNT structures deserves further study.

Ultrathin high-resolution printing via nanoscale control of ink transfer

Ink transfer from the nanoporous stamp to solid substrates occurs by wetting of the ink to the substrate upon contact of nanofibers at the interface. That is, when the wet stamp contacts the target substrate under applied pressure, the nanofibers at the top of the stamp provide physical bridges for the liquid ink to wet the target substrate. These ensuing liquid bridges may coalesce as the pressure is increased and more fibers come into contact with the substrate. Then, as the stamp retracts, a portion of the ink will remain on the substrate, and upon evaporation of the solvent, a thin layer of NPs results.

Accordingly, to achieve uniform ink transfer, the wet stamp must contact the substrate with a sufficient uniform pressure while retaining the ink within the bounds of the nanoporous microstructure. In Fig. 3A, we illustrate the nanoscopic view of inked CNT stamp and its contact against the target substrate. The top surface of a stamp microstructure with well-confined ink consists of the free surface (>90%) held by the network of polymer-coated CNTs (diameter, 10 to 50 nm; spacing, ~100 nm). The intrinsic height variance of the CNT network (~10 to 100 nm) causes roughness of the free surface where the ink is pinned to the tips of the coated CNTs. When the stamp contacts the substrate, the compliance of the CNTs allows the stamp to conform to the roughness of the target substrate at moderate pressure. Increased contact pressure ensures conformal contact and drives the confined ink to wet the target surface more uniformly, yet excessive pressure can cause overprinting (that is, loss of fidelity) and/or failure of the stamp by buckling, as discussed later.

A mechanical model of the compliant stamp surface allows us to estimate the required pressure for conformal contact that results in uniform ink transfer. We assume that the tips of the pPFDA-CNTs have normally distributed positions (l_{CNT}) with a standard deviation of σ_l relative to a nominal plane; thus, the probability density of the surface heights is

$$\phi(l_{CNT}) = \frac{1}{\sigma_l\sqrt{2\pi}} \exp\left(-\frac{l_{CNT}^2}{2\sigma_l}\right) \quad (1)$$

When two surfaces are in contact at a distance (d) between their nominal planes, the applied pressure (p) is supported by the pPFDA-CNT fibers in contact over the area (A)

$$p = \frac{1}{A}\sum_i^{n_c} P_{CNT,i} = \frac{1}{A}\sum_i^{n_c} k_{CNT}\delta_{CNT,i} = \frac{n}{A}\int_d^\infty k_{CNT}(l_{CNT} - d)\cdot\phi(l_{CNT})dl_{CNT}$$
$$= \frac{k_{CNT}\sigma_l}{\sqrt{2\pi}\lambda_{CNT}^2}\left[\exp\left(-\frac{d^2}{2\sigma_l^2}\right) - \sqrt{\frac{\pi}{2}}\frac{d}{\sigma_l}\left\{1 - \mathrm{erf}\frac{d}{\sqrt{2}\sigma_l}\right\}\right] \quad (2)$$

Here, $P_{CNT,i}$ is the load supported by ith pPFDA-CNT fiber in contact, n_c is the number of fibers in contact, n is the total number of fibers on the stamp surface ($\cong A/\lambda_{CNT}^2$), k_{CNT} is the stiffness of a single pPFDA-CNT fiber, $\delta_{CNT,i}$ is the deformation distance of ith fiber in contact (= $l_{CNT,i} - d$), and λ_{CNT} is the average spacing between the fibers. Moreover, the contact ratio at the given distance d will be

$$\frac{n_c}{n} = \int_d^\infty \phi(l_{CNT})dl_{CNT} = \frac{1}{2}\left\{1 - \mathrm{erf}\frac{d}{\sqrt{2}\sigma_l}\right\} \quad (3)$$

Therefore, the contact ratio is determined by the contact pressure, stiffness (surface compliance), surface height variation, and spacing of the pPFDA-CNT fibers. In Fig. 3B, we show the predicted relationship between contact ratio and pressure for the CNT stamp. The CNT-CNT spacing (λ_{CNT} ~ 100 nm) was measured from SEM images (fig. S4), σ_l ~ 50 nm was determined from AFM analysis (fig. S3), and k_{CNT} ~ 2.7 mN/m was calculated from the nanoindentation curve ($k_{CNT} \sim E_C\lambda_{CNT}^2/H$, where H is the CNT average height used in the uniaxial compression test; Fig. 2D). The required contact pressure for the CNT stamp to conformally contact the target substrate (>99% contact ratio) is estimated to be ~28 kPa.

To validate the model, we measure the relationship between applied pressure and the ink transfer ratio, which is defined as the area of Ag NP ink printed on a glass substrate (root mean square roughness, ~2 nm) divided by the area of the stamp pattern. At lower pressure (<28 kPa), incomplete transfer is observed within each microscale stamp feature. At moderate pressure (28 to 150 kPa), the printed features match the stamp patterns, indicating that the contact is uniform. At high pressure (>150 kPa), overprinting is observed where the size of the printed features exceeds the stamp feature sizes, and there is a significant loss of shape fidelity. This indicates that excessive deformation of the stamp surface and/or buckling of the CNT features is forcing excessive ink onto the substrate where it spreads laterally outward from the contact area. Without plasma etching of the surface layer, conformal surface contact cannot be achieved at contact pressure lower than the buckling limit of the coated CNT forest (~150 kPa).

For these reasons, control of the resolution and fidelity (for example, edge roughness and corner radius) of printed features depends on the stamp preparation (for example, CNT microstructure geometry, surface roughness, mechanical properties, and surface treatment) and the magnitude and uniformity of the contact pressure. In addition, the amount of ink loaded onto the stamp also significantly affects the shape of printed features. The sequence of steps for ink loading and printing to achieve micrometer-resolution printing is illustrated in Fig. 3D. Upon spin coating, the ink is drawn into the CNT microstructures by capillary wicking, and the excess ink is mostly removed from the stamp by the centrifugal forces during the spinning process. However, we find that a slight amount of excess ink is present on the stamp surface. When this stamp is used to print, the excess ink spreads upon contact, resulting in greater width and corner roundness

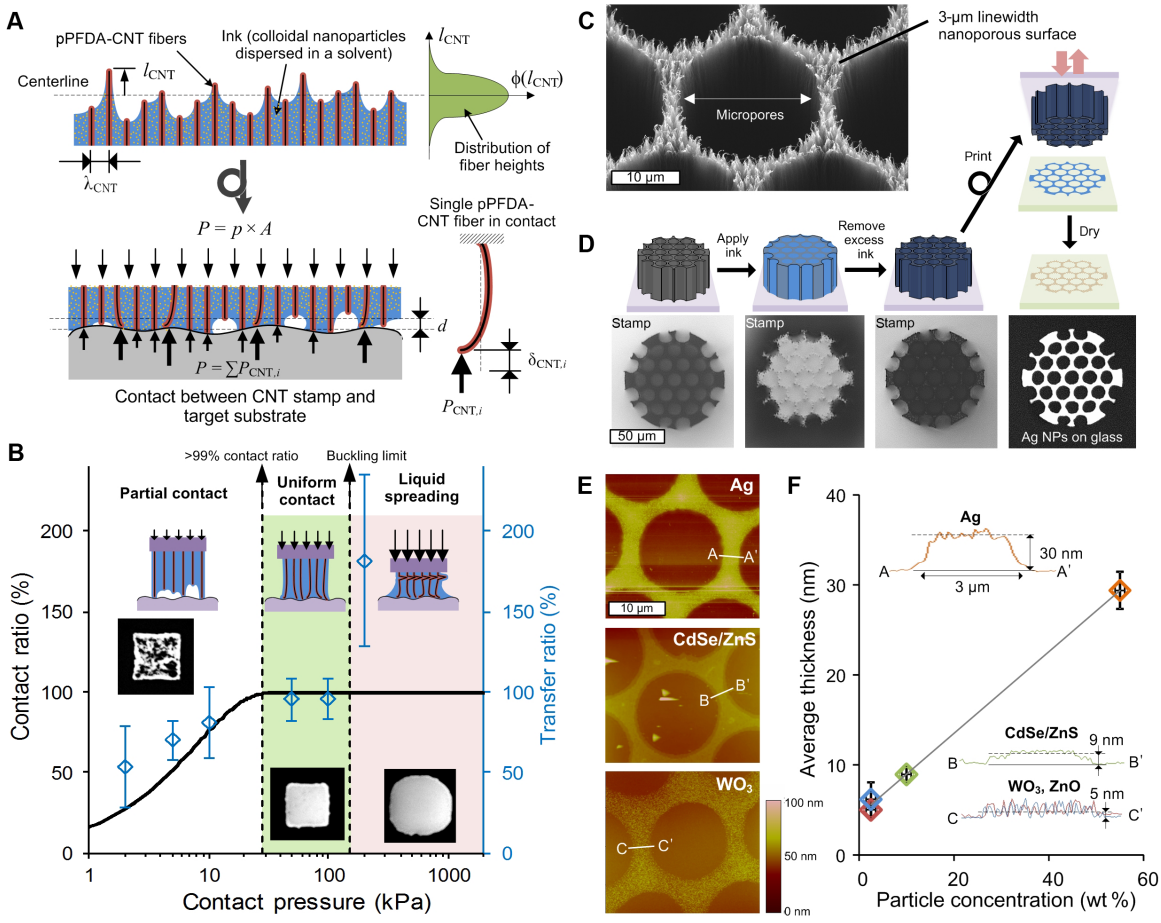

Fig. 3. Control of ink loading and transfer to achieve ultrathin high-resolution flexoprinting. (**A**) Schematic (not to scale) of nanoscopic view of CNT stamp surface after loading with ink and upon contact with target substrate surface. (**B**) Ratio of contact between CNT surface fibers and target substrate (black solid line; contact model shown in Eqs. 2 and 3) and contact ratio of colloidal ink transferred onto a glass substrate (gray diamonds with error bars; experimental results) versus applied pressure. (**C**) Magnified SEM image of CNT stamp feature (fabricated as in Fig. 2) having a honeycomb structure with minimum internal linewidth of 3 μm. (**D**) Schematics and optical microscope images of a CNT stamp feature, after spin coating of ink, after removal of the excess ink by contact against a nonpatterned CNT forest and the resulting printed pattern on a glass substrate after solvent evaporation. (**E**) AFM images of printed honeycomb pattern of Ag NPs, CdSe/Zn QDs, and WO_3 NPs. (**F**) Cross-sectional profiles and a plot of average thickness versus ink concentration of printed lines (width, 3 μm) for 2.5 wt % (Al-doped ZnO, red; WO_3 NPs, blue), 10 wt % (CdSe/Zn QDs, green), and 55 wt % (Ag NPs, orange) inks.

of the printed features compared to the stamp and an overall loss of pattern fidelity (fig. S8). To solve this problem, before printing, we contact the wet stamp with a nonpatterned, plasma-treated CNT forest. The nonpatterned forest, which is porous and wettable by the ink, draws the excess ink from the stamp surface while leaving the stamp features neatly filled and ready for printing. When the CNT stamp is then used for printing, uniform ink transfer is achieved by relying on the formation of nanoscale contact points across the surface of each microscale stamp feature, therefore replicating the shapes of the stamp features with high accuracy.

After printing the wet ink, solvent evaporation results in an ultrathin, uniform layer of NPs matching the stamp feature geometry. For example, printed Ag lines (width, 20 μm) exhibit uniform thickness of ~40 nm, with surface roughness of only 1.2 nm (fig. S9). Together, we explored printing of four different commercially available inks (see Materials and Methods): ZnO (particle size, 8 to 16 nm), WO_3 (particle size, 11 to 21 nm), CdSe/ZnS core-shell type QDs (particle size, 2 to 6 nm), and Ag (particle size, <10 nm). The inks are composed of NPs dispersed in a low-volatility solvent, either tetradecane or a mixture of 2-propanol and propylene glycol, which exhibits high wettability (contact angle, <90°) on both the stamps and the target substrates. Using the same stamp design (CNT-CNT spacing and surface stiffness and roughness) and inking-printing sequence (initial ink load and printing pressure and speed), we find that the volume of ink transferred to the substrate is the same for all inks (Fig. 3E). Thus, the particle concentration in the ink solution mainly determines the final average thickness after the solvent evaporates (Fig. 3F). The printed particles form a monolayer when the concentration is low (~2.5 wt %), whereas they form multiple layers when the concentration is high (>10 wt %).

Unlike inkjet printing, the "coffee ring" effect is absent in patterns printed using nanoporous stamps; this is because the local evaporation rates across the uniformly transferred thin ink layer are not significantly different, and therefore, there is no capillary flow induced during solvent evaporation. As a result, the dimensions of the printed features closely match the stamp features, and the particle layers are

highly uniform within the printed feature. Printing of these thin, uniform layers is attractive for electronic device fabrication, such as thin-film transistors, where a variety of materials need to be deposited and patterned in spatially registered layers (*46*, *47*).

Scalable printing of electronic materials

Using the above-mentioned NP inks, we printed a diverse range of patterns representing the unique capability of nanoporous stamps to replicate narrow, wide, sharp, and smoothly curved shapes (Figs. 1D and 4A) and to print patterns with widely differing cross-sectional dimensions in close proximity. For example, the array of Ag square patterns with side length of ~25 μm corresponds to ~720 dpi, which is the subpixel size of "Retina" displays. The half-circle array and curved lines of QDs represent the capability to print patterns with corners having a radius of ~3 μm and linewidth and spacing smaller than 10 μm. Also, the honeycomb patterns achieve uniform microscale fidelity over large areas. The lateral dimensions of QD and Ag NP honeycomb pattern are identical; however, their average heights are different because of different particle concentrations, as shown in Fig. 3F. The printed Ag honeycombs and straight lines have line edge roughness of ~0.2 μm, which is 10-fold lower than the typical edge roughness (~2.0 μm) achieved by gravure printing (*21*). The corner radius and edge roughness are mutually determined by the corresponding attributes of the catalyst film initially patterned for CNT growth and the approximate spacing of coated CNTs along the edges of the stamp features after the post-processing steps.

To demonstrate how these process attributes translate to material performance, we first characterized the electrical properties of Ag lines, which were annealed to form solid features from the printed NP layers. After annealing for 10 min at 200°C, the conductivity measured across

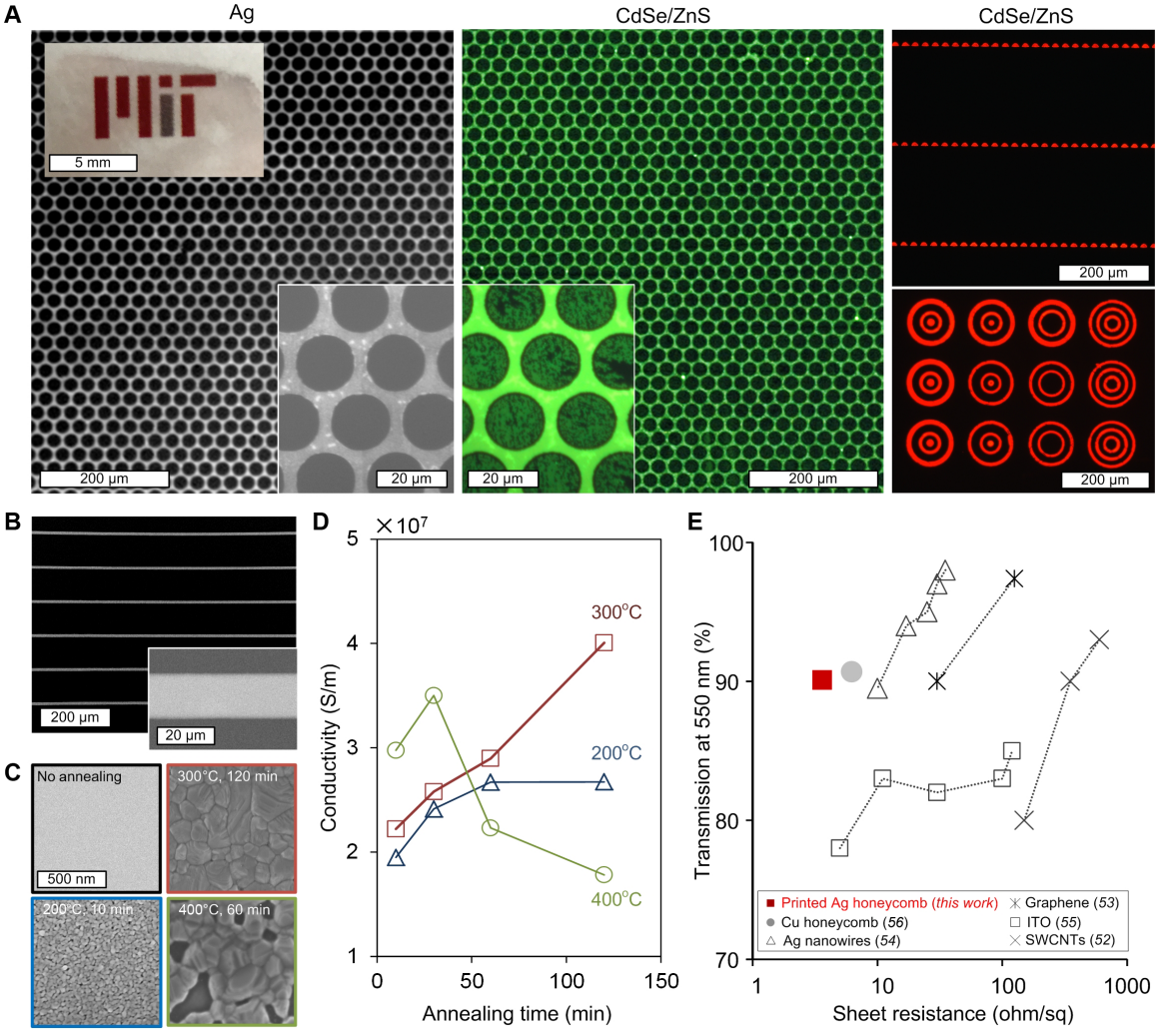

Fig. 4. Functional large-area printing of electronic materials. (**A**) Optical images of Ag honeycomb patterns having a minimum linewidth of 3 μm between adjacent holes printed on glass slides, along with fluorescence images of CdSe/ZnS core-shell QDs, printed as large-area honeycomb patterns [fluorescent emission peak, ~ 540 nm (green)] and arrays of half circles having a diameter of 15 μm with spacing of 5 μm (horizontal) and 250 μm (vertical), concentric circles with linewidth and spacing of 5 to 10 μm [fluorescent emission peak, ~620 nm (red)]. SEM images of printed Ag line array (**B**) (linewidth, 20 μm; pitch, 200 μm) and SEM images showing evolution of printed Ag morphology after sintering (**C**) at indicated times and temperatures along with corresponding conductivity values (**D**). (**E**) Comparison of the sheet resistance and transmission (at wavelength of 550 nm) values of the printed Ag honeycomb (solid red square) to other transparent materials reported in literature, including Cu honeycomb grids with Al-doped ZnO layer (*56*), Ag nanowires (*54*), graphene (*53*), indium tin oxide (ITO) (*55*), and single-walled carbon nanotubes (SWCNTs) (*52*).

an array of lines (20 μm wide with pitch of 200 μm) reached 1.9 × 10^7 S/m, and after annealing for 120 min at 300°C, the conductivity increased to 4.0 × 10^7 S/m (Fig. 4D). These values represent approximately 30 and 60% of the conductivity of bulk Ag (6.3 × 10^7 S/m), respectively. SEM imaging (Fig. 4C) shows how the nanoscale morphology of the printed features evolves during thermal annealing; at shorter times and lower temperatures, voids are present, whereas the highest conductivity is accompanied by a void-free nanocrystalline surface texture. If the annealing conditions are too aggressive, the resistivity rises because of the dewetting of the Ag film, resulting in local disconnections between the metallic particles. At a commercial scale, it would be possible to adopt much faster annealing methods, such as continuous flash exposure (*48*). For example, sintering by combined low-pressure Ar plasma and microwave flash for less than 10 min resulted in conductivity of 60% of bulk silver (*49*).

One important application of printed conductive networks is transparent electrodes, which are used in light-emitting diodes, liquid crystal displays, touch-screen panels, solar cells (*50*, *51*), and numerous other devices. For all these applications, cost-effective fabrication of electrodes with high conductivity and transparency is essential. Using the CNT honeycomb stamp, we realize a printed Ag honeycomb having transparency of 94% (at wavelength of 200 to 800 nm; fig. S10), along with sheet resistance of 3.6 ohm/sq after thermal annealing. The measured sheet resistance is half that of indium tin oxide at 90% transparency and one-tenth the value reported for Ag nanowire networks at 90% transparency (Fig. 4E) (*52*–*55*). Transparent metal grids can be made by other methods; for example, Kim *et al.* (*56*) demonstrated copper honeycomb patterns with an Al-doped ZnO capping layer, having 91% transparency at 6.2 ohm/sq. However, several steps, including sputtering, ultraviolet lithography, and wet etching, were required. Flexographic printing using nanoporous stamps is a single-step ambient process that can be conducted continuously and at high speed.

Moreover, using a custom-built plate-to-roll (P2R) printing apparatus in our laboratory (Fig. 5A), we show that Ag honeycomb patterns can be directly printed to PET films at speeds of up to 0.2 m/s (Fig. 5B). This speed is currently limited by the linear motion stage (ANT130-L, Aerotech) that was selected for precision coordination of the rotary and linear axes. At 0.2 m/s, the contact time of the stamp against the substrate is approximately 250 μs, which is far greater than the liquid-spreading time scale driven by surface wetting ($\eta_{ink}\lambda_{CNT}/\gamma_{ink}$ ~ 0.1 μs, where η_{ink} and γ_{ink} are the viscosity and the surface tension of the ink, respectively). Accordingly, we expect that the printing speed can surpass industrial standards (>1 m/s) upon adaptation to roll-to-roll flexographic printing equipment that has even higher-speed motion capability.

DISCUSSION

We have shown that nanoporous stamps made from polymer-coated CNT forests can potentially address two critical limitations of existing printing methods for electronic materials: direct printing of features with micrometer-scale lateral dimensions and fine edge roughness, and attainment of highly uniform thickness in the sub-100 nm range. The key functionality of the new stamp comes from its mechanical compliance, along with its high porosity. The stamp pore size (characteristic length of d_{pore}) is larger than the electrically functional NPs to be printed ($d_{particle}$) but smaller than the stamp features (w_{stamp}). For the ink particles to remain well dispersed within the wet stamp, the pores within the stamp should be much larger than the particles ($d_{particle} << d_{pore}$). In addition, for uniform ink transfer relative to the size of the stamp feature (and thus, the resulting printed feature), the pores must be significantly smaller than the stamp features ($d_{pore} << w_{stamp}$). We find that engineered CNT stamps having pores of ~100 nm can uniformly print ink particles of ~10 nm using stamp features with lateral size approaching 1 μm.

As a potential indication of promise, we compare (Fig. 5, C and D) the performance of nanoporous flexographic printing to other techniques, which span from laboratory to industrial scales, and involve widely different material transfer mechanisms. The high-speed capability of conventional printing technologies including flexography arises from their rapid material transfer mechanism driven by wetting and spreading of solvent-based inks, and this is critical to their commercial viability. By leveraging this mechanism at the nanoscale, the rate of our process already exceeds that of all known methods for micrometer resolution printing (Fig. 5C). Soft lithography, including microcontact printing (μCP) and microtransfer/nanotransfer printing (μTP/nTP), has been used to pattern many materials with micrometer and submicrometer feature size using elastomeric stamps (*25*, *26*, *57*–*59*); however, material transfer must be carefully guided by the intrinsic surface energies of the stamp and receiving substrate with chemical, thermal, and/or viscoelastic modulation. As a result, the rate of these methods is limited to ~0.01 m/s. We also recognize that tip- and nozzle-based printing technologies, including dip-pen nanolithography (DPN) (*27*, *30*, *60*, *61*), direct writing (*62*, *63*), and electrohydrodynamic (EHD) printing (*28*, *64*), have achieved superior resolution, including resolution approaching ~10 nm for DPN of molecular inks. However, the scalability of tip-based methods, even for parallel tip arrays, is limited by their pointwise nature and low transfer speed (~0.1 mm/s or less), which is not suitable for large-area electronics manufacturing. Nanoporous flexography also achieves area-normalized ink transfer volumes of ~0.5 fl/μm (Fig. 5D), which is ~100-fold less than current flexography methods and ~10-fold less than recently published advances in gravure and inkjet printing (*12*, *21*). This results in direct printing of ultrathin films.

At present, the limitation to printing smaller features using nanoporous flexography is the uniformity of CNT growth in our CVD system (*65*); however, we anticipate that reductions in the CNT stamp feature size in concert with above design considerations could enable further advances in printing resolution. For example, stamps comprising single-walled CNTs that have significantly smaller diameter (1 to 2 nm) and spacing (~10 to 20 nm) (*66*) could be suitable for printing submicrometer features and for improving edge quality. Here, conventional laser-written lithography masks and manual exposure tools were used to create the CNT catalyst patterns with a resolution limit of ~2 to 3 μm, which defines the minimum printed feature size (fig. S2). Higher-resolution patterning methods could be used to create much finer CNT stamp features. The relationship between stamp geometry and porosity, ink properties, and process parameters on the printed feature thickness also requires further study.

Another key challenge in industrialization of μCP/nTP methods is that elastomeric stamp features are prone to buckling or roof collapse, and this critically limits the process reliability and the shapes of features that can be printed over large areas (*67*–*70*). Because compliant CNT microstructures are grown on rigid substrates, our CNT stamps do not suffer from roof collapse even for patterned features

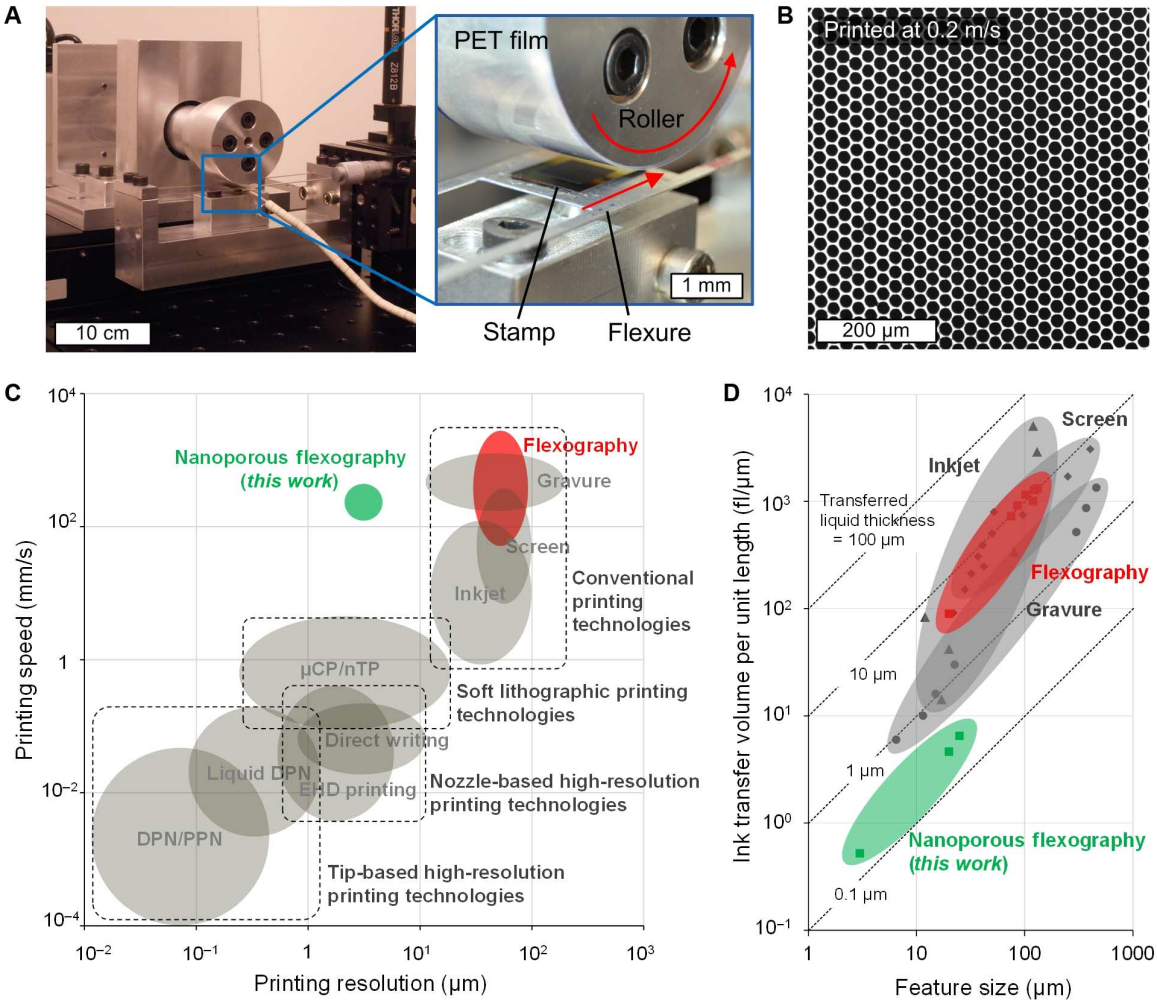

Fig. 5. High-speed printing and process performance metrics. (**A**) Custom-built desktop P2R printing system with a CNT stamp attached on a flat flexure and a PET film attached to a roller with a diameter of 5 cm. (**B**) Optical microscope image of Ag honeycomb pattern with minimum internal linewidth of 3 μm printed on a PET substrate at a printing speed of 0.2 m/s using the P2R system. (**C**) Comparison of speed and resolution of conventional printing technologies for electronically functional materials. Conventional processes include flexography, gravure, screen, and inkjet (*8*–*24*). Soft lithography includes μCP and nTP (*25*, *26*, *57*–*59*, *67*–*70*); Nozzle-based high-resolution printing methods include direct writing and EHD printing (*27*, *62*–*64*). Tip-based methods include DPN and polymer pen lithography (PPN) (*28*, *29*, *60*, *61*). (**D**) Comparison of volume per unit length, lateral feature size, and thickness of ink that transfers to the substrate by single print (by mechanical contact or drop) in conventional printing technologies (*8*–*24*), compared to nanoporous flexographic printing, as shown in this paper.

with large spacing or low aspect ratio. Moreover, CNT forest microstructures have been shown to withstand millions of compression loading cycles (*71*) and can also be engineered to recover from large compressive deformations (in some cases, >70%) (*72*–*74*). We find that the conformal coating of the CNTs with the low-surface energy polymers enables the stamp features to withstand extended cyclic loading that far exceeds the critical pressure required for printing (fig. S11) because of reversible buckling at the base, which does not disturb the contact mechanics of the stamp surface. As a preliminary demonstration, we find that 100 printing cycles using the same stamp under identical printing conditions do not result in noticeable degradation of the surface (fig. S12).

For commercial applications, it will also be necessary to establish continuous (that is, roll-to-roll) printing using nanoporous stamps and to fabricate the stamps in cylindrical formats that are compatible with high-speed printing equipment. To do so, the CNT growth catalyst could be deposited directly onto the roll before CNT growth, or CNTs could be grown on large-area flat substrates (for example, glass plates) and then transferred to a flexible substrate (*75*). In addition, to avoid the use of photolithography for stamp fabrication, CNT forests can be grown from a nonpatterned catalyst layer and then structured using subtractive methods (*76*, *77*) such as laser ablation.

CONCLUSION

In conclusion, we show that microstructured nanoporous stamps comprising polymer-coated CNT arrays enable direct micrometer-resolution flexographic printing of colloidal inks, surpassing the documented resolution limits of industrial flexographic printing methods by at least 10-fold. The local control of ink transfer via conformal nanoscale contact of the wet porous surface suggests that further miniaturization of the process will be possible by engineering the nanostructure of the stamp and both its chemistry and mechanics. Moreover, the lithographic and CVD processes used to prototype the nanoporous stamps

are scalable to industrial methods for roll-to-roll tool fabrication. In addition to having micrometer-scale resolution, the direct printing of patterns with uniform nanoscale thickness will be greatly beneficial to scalable manufacturing of devices such as high-performance transistors, low-cost wireless sensors, and complex metasurfaces.

MATERIALS AND METHODS

Stamp fabrication

For the growth of vertically aligned CNTs, an Al_2O_3/Fe catalyst layer was first patterned on 100 mm (100) silicon wafers coated with 300 nm of thermally grown SiO_2 by liftoff processing using photolithography, followed by ultrasonic agitation in acetone. The supported catalyst layer, 10 nm of Al_2O_3 and 1 nm of Fe, was sequentially deposited by electron beam physical vapor deposition. The wafer with the deposited catalyst was diced into ~2-cm × 2-cm pieces and placed in the quartz tube furnace for the CNT growth. The growth recipe started with flowing 100/400 standard cubic centimeter per minute (SCCM) of He/H_2 while heating the furnace up to 775°C over 10 min (ramping step), and then maintaining the temperature at 775°C for 10 min with the same gas flow rates (annealing step). Then, the gas flow was changed to 100/400/100 SCCM of $C_2H_4/He/H_2$ at 775°C for CNT growth for the selected duration. The typical growth rate was ~100 μm/min, and the CNTs were multiwalled with a mean diameter of ~10 nm, with 0.45 of coefficient of variation at the top of the forest, as we had previously measured by x-ray scattering (*33*). After the growth, the furnace was cooled down to <100°C at the same gas flow and finally purged with 1000 SCCM of He for 5 min. For plasma etching, the CVD-grown CNTs were exposed to an oxygen plasma with 80/20 of Ar/O_2 gas flow for 5 min at 50 W and 200 mtorr pressure using a Diener Femto Plasma system.

For conformal polymer coating, iCVD polymerization was carried out in a custom-built cylindrical reactor (diameter, 24.6 cm; height, 3.8 cm) with an array of 14 parallel chromoalloy filaments (Goodfellow) suspended 2 cm from the stage. The reactor was covered with a quartz top (2.5 cm thick) that allows real-time thickness monitoring by reflecting a 633-nm He-Ne laser source (JDS Uniphase) off the substrate/polymer and recording the interference signal intensity as a function of time. The reactor was pumped down by a mechanical Fomblin pump (Leybold, Trivac), and the pressure was monitored with a MKS capacitive gauge. The liquid monomer [1*H*,1*H*,2*H*,2*H*-perfluorodecyl acrylate (PFDA) 97%; Sigma-Aldrich] and the initiator [tert-butyl peroxide (TBPO) 98%; Sigma-Aldrich] were used as received without further purification. TBPO was kept at room temperature (T_f = 25°C) and was delivered into the reactor through a mass flow controller (1479 MFC, MKS Instruments) at a constant flow rate of 1 SCCM in process A (in situ grafting) and 3 SCCM and 1 SCCM in DVB and PFDA polymerization during process B (two-step deposition), respectively. Initiator radicals (TBO) were created by breaking only the labile peroxide bond of the TBPO at filament temperature of T_f = 250°C during iCVD polymerization. The PFDA monomer was vaporized in glass jars that are heated to 80°C and then introduced to the reactor through needle valves at constant flow rates of 0.2 SCCM. The substrate temperature was kept at T_s = 30°C (within ±1°C) using a recirculating chiller/heater (NESLAB RTE-7). All of the temperatures were measured by K-type thermocouples (Omega Engineering). The working pressure was maintained at 60 mtorr using a throttle valve (MKS Instruments). At the end, an ultrathin layer of pPFDA (approximately 30 nm thick) was deposited within 25 min of deposition time. The thickness of the pPFDA, deposited on to a control silicon substrate during iCVD polymerization, was also measured using ellipsometry. Finally, the pPFDA-coated CNTs were again exposed to an oxygen plasma for 30 s at 30 W and pressure of 200 mtorr.

Inking/printing

For inking, 50 to 200 μl of ink was applied on the stamp by a pipette, and then, the stamp was spun at 1500 rpm for 0.5 to 5 min. A plasma-treated, nonpatterned CNT forest was brought into contact against the top surface of the stamp by its own weight for 1 to 5 s. For plate-to-plate printing, the target substrate (microscope glass slide and PET film attached to glass slide, etc.) contacted the stamp at ~50 to 100 kPa of contact pressure for 1 to 5 s. Appropriate normal load was applied by a dead weight placed above the substrate. For P2R printing, the target substrate (PET film) was attached to a roller with diameter of 5 cm and rolled over the inked stamp with controlled force (corresponding pressure to be ~50 to 100 kPa) and speed (corresponding linear velocity to be 1 to 200 mm/s) using a laboratory-built desktop system. Microslide glasses (surface roughness, ~1 to 2 nm; VWR International LLC) and PET film 100 μm thick (average roughness, ~6 to 10 nm; McMaster-Carr) were used as the target substrates. The Ag ink used in this study was composed of silver NPs dispersed in tetradecane (736511, Sigma-Aldrich). The particle concentration was 50 to 60 wt % with particle sizes less than 10 nm. The QD ink was composed of COOH-functionalized CdSe/ZnS core-shell type QDs (748056 and 790192, Sigma-Aldrich) dispersed in tetradecane (172456, Sigma-Aldrich) by 3-min sonication. The particle concentration was ~10 wt %. The ZnO and WO_3 ink was composed of crystalline Al-doped ZnO (3.15 mole percent Al; work function, ~4.1-4.5 eV; 808172, Sigma-Aldrich) and crystalline WO_3 (work function, ~5.3 to 5.7 eV; 807753, Sigma-Aldrich) NPs dispersed in 2-propanol and propylene glycol. The particle concentrations for both inks were 2.5 wt % with particle sizes of 8 to 16 nm for ZnO and 11 to 21 nm for WO_3.

Characterization

The mechanical properties of stamp microstructures were characterized using a nanoindenter (Hysitron TI 900). To measure the surface properties, a 10-μm radius tip was indented to a maximum depth of 1 μm, and the surface modulus was determined via Oliver-Pharr method from the load-displacement curve. To characterize the bulk properties, a 100-μm flat tip was indented to a maximum depth of 4.5 μm, and compressive modulus was determined from the unloading curve assuming a uniaxial compression. Micropillars having a diameter of 100 μm and a height of ~150 μm were used for all the indentation tests. For wetting/dewetting tests, the arrays of the micropillars were wetted by 10 to 100 μl of water droplet and imaged by a high-speed camera. The optical microscope (Zeiss AxioCam) and fluorescence microscope (Zeiss AxioSkop 2 MAT) images of printed ink patterns were taken within a few days after printing. The SEM (Zeiss Merlin) and AFM (Veeco Metrology Nanoscope IV) images of printed ink patterns were taken 3 to 10 days after printing or after sintering at 200°, 300°, 400°, and 500°C for 10, 30, 60, and 120 min on a hot plate. To measure the conductivity of printed silver NPs, 15 line structures having a width of 20 μm, spacing of 200 μm, and length of 4 mm were printed on silicon substrates. Electrically conductive silver epoxy (Electron Microscopy Sciences) was used to connect each end of the line structures. Then, resistances were measured by a multimeter (National Instruments VirtualBench) from one end to another, and conductivities were calculated from the average resistance of 15 lines.

To measure the transmission and sheet resistance, 1.5-cm × 1.5-cm honeycomb pattern arrays were printed on microscope glass slides. Optical transmissivity was measured using a spectrophotometer (Cary UV-visible-NIR transmission/reflectance spectrophotometer), and the sheet resistances were measured using a four-point probe (Jandel RM3-AR).

SUPPLEMENTARY MATERIALS

Supplementary material for this article is available at http://advances.sciencemag.org/cgi/content/full/2/12/e1601660/DC1

fig. S1. SEM images of the cross section of a CNT microstructure after infiltration of silver NP ink and dried at ambient conditions for 3 days.
fig. S2. SEM images (30° tilted view) of a square pattern of Fe (1 nm)/Al_2O_3 (10 nm) catalyst film and CVD-grown vertically aligned CNT on the same catalyst pattern.
fig. S3. SEM and AFM images of the top surface of a CNT forest microstructure (as-grown).
fig. S4. SEM images of the top surface of a circular (diameter, 100 μm) CNT microstructure at each fabrication stage.
fig. S5. Comparison of a square micropattern at each stage of stamp fabrication and the printed Ag pattern from this stamp feature.
fig. S6. Comparison between as-grown and pPFDA-coated CNT micropillars.
fig. S7. Optical image of a silver NP ink droplet on an array of CNT pillars (diameter, 100 μm) coated with pPFDA before the second plasma treatment (Fig. 2).
fig. S8. Schematics and optical microscope images.
fig. S9. AFM images and schematics (not to scale) of lines printed using stamp.
fig. S10. Transmission spectrum of printed Ag honeycomb pattern on a glass plate.
fig. S11. Uniaxial stress-strain curves and SEM images of the base regions CNT microstructures.
fig. S12. Optical microscope images of a nanoporous honeycomb stamp microstructure before and after multiple prints of the Ag ink.
video S1. Wetting/dewetting tests on plasma-etched CNT micropillars.
video S2. Wetting/dewetting tests on plasma-treated pPFDA-CNT micropillars.
video S3. Wetting/dewetting tests on pPFDA-CNT micropillars.

REFERENCES AND NOTES

1. R. Whitfield, A. Farrer, S. J. Vainker, J. Rawson, *Caves of the Thousand Buddhas: Chinese Art from the Silk Route* (The British Museum Press, London, U.K., 1990).
2. Korean Spirit and Culture Promotion Project, *Fifty Wonders of Korea* (Korean Spirit andCulture Promotion Project, Seoul, Republic of Korea, 2008).
3. H. Kipphan, *Handbook of Printed Media: Technologies and Production Methods* (Springer, 2001).
4. R. F. Service, Patterning electronics on the cheap. *Science* **278**, 383–384 (1997).
5. S. R. Forrest, The path to ubiquitous and low-cost organic electronic appliances on plastic. *Nature* **428**, 911–918 (2004).
6. R. Want, RFID: A key to automating everything. *Sci. Am.* **290**, 56–65 (2004).
7. OE-A roadmap for organic and printed electronics (Organic and Printed Electronics Association, Frankfurt, Germany, ed. 6, 2015).
8. P. F. Moonen, I. Yakimets, J. Huskens, Fabrication of transistors on flexible substrates: From mass-printing to high-resolution alternative lithography strategies. *Adv. Mater.* **24**, 5526–5541 (2012).
9. S. Khan, L. Lorenzelli, R. S. Dahiya, Technologies for printing sensors and electronics over large flexible substrates: A review. *IEEE Sens. J.* **15**, 3164–3185 (2015).
10. D. Deganello, J. A. Cherry, D. T. Gethin, T. C. Claypole, Patterning of micro-scale conductive networks using reel-to-reel flexographic printing. *Thin Solid Films* **518**, 6113–6116 (2010).
11. F. C. Kreb, J. Fvenbo, M. Jørgensen, Product integration of compact roll-to-roll processed polymer solar cell modules: Methods and manufacture using flexographic printing, slot-die coating and rotary screen printing. *J. Mater. Chem.* **20**, 8994–9001 (2010).
12. H.-H. Lee, K.-S. Chou, K.-C. Huang, Inkjet printing of nanosized silver colloids. *Nanotechnology* **16**, 2436–2441 (2005).
13. M. Singh, H. M. Haverinen, P. Dhagat, G. E. Jabbour, Inkjet printing—Process and its applications. *Adv. Mater.* **22**, 673–685 (2010).
14. K. Fukuda, Y. Takeda, Y. Yoshimura, R. Shiwaku, L. T. Tran, T. Sekine, M. Mizukami, D. Kumaki, S. Tokiot, Fully-printed high-performance organic thin-film transistors and circuitry on one-micron-thick polymer films. *Nat. Commun.* **5**, 4147 (2014).
15. F. C. Krebs, T. Tromholt, M. Jørgenen, Upscaling of polymer solar cell fabrication using full roll-to-roll processing. *Nanoscale* **2**, 873–886 (2010).
16. R. Faddoul, N. Reverdy-Bruas, A. Blayo, Printing force effect on conductive silver tracks: Geometrical, surface, and electrical properties. *J. Mater. Eng. Perform.* **22**, 640–649 (2013).
17. D. Erath, A. Filipović, M. Retzlaff, A. K. Goetz, F. Clement, D. Biro, R. Preu, Advanced screen printing technique for high definition front side metallization of crystalline silicon solar cells. *Sol. Energy Mater. Sol. Cells* **94**, 57–61 (2010).
18. W. J. Hyun, S. Lim, B. Y. Ahn, J. A. Lewis, C. D. Frisbie, L. F. Francis, Screen printing of highly loaded silver inks on plastic substrates using silicon stencils. *ACS Appl. Mater. Interfaces* **7**, 12619–12624 (2015).
19. J. Noh, D. Yeom, C. Lim, H. Cha, J. Han, J. Kim, Y. Park, V. Subramanian, G. Cho, Scalability of roll-to-roll gravure-printed electrodes on plastic foils. *IEEE Trans. Electron. Packag. Manuf.* **33**, 275–283 (2010).
20. M. Jung, J. Kim, J. Noh, N. Lim, C. Lim, G. Lee, J. Kim, H. Kang, K. Jung, A. D. Leonard, J. M. Tour, G. Cho, All-printed and roll-to-roll-printable 13.56-MHz-operated 1-bit RF tag on plastic foils. *IEEE Trans. Electron Devices* **57**, 571–580 (2010).
21. H. Kang, R. Kotsomboonloha, J. Jang, V. Subramanian, High-performance printed transistors realized using femtoliter gravure-printed sub-10 μm metallic nanoparticle patterns and highly uniform polymer dielectric and semiconductor layers. *Adv. Mater.* **24**, 3065–3069 (2012).
22. S. G. Higgins, F. L. Boughey, R. Hills, J. H. G. Steinke, B. V. O. Muir, A. J. Campbell, Quantitative analysis and optimization of gravure printed metal ink, dielectric, and organic semiconductor films. *ACS Appl. Mater. Interfaces* **7**, 5045–5050 (2015).
23. B. Derby, Inkjet printing of functional and structural materials: Fluid property requirements, feature stability, and resolution. *Annu. Rev. Mater. Res.* **40**, 395–414 (2010).
24. M. K. Kwak, K. H. Shin, E. Y. Yoon, K. Y. Suh, Fabrication of conductive metal lines by plate-to-roll pattern transfer utilizing edge dewetting and flexographic printing. *J. Colloid Interface Sci.* **343**, 301–305 (2010).
25. J. L. Wilbur, A. Kumar, E. Kim, G. M. Whitesides, Microfabrication by microcontact printing of self-assembled monolayers. *Adv. Mater.* **6**, 600–604 (1994).
26. Y.-L. Loo, R. L. Wilett, K. W. Baldwin, J. A. Rogers, Interfacial chemistries for nanoscale transfer printing. *J. Am. Chem. Soc.* **124**, 7654–7655 (2002).
27. J.-U. Park, M. Hardy, S. J. Kang, K. Barton, K. Adair, D. k. Mukhopadhyay, C. Y. Lee, M. S. Strano, A. G. Alleyne, J. G. Georgiadis, P. M. Ferreira, J. A. Rogers, High-resolution electrohydrodynamic jet printing. *Nat. Mater.* **6**, 782–789 (2007).
28. R. D. Piner, J. Zhu, F. Xu, S. Hong, C. A. Mirkin, "Dip-pen" nanolithography. *Science* **283**, 661–663 (1999).
29. F. Huo, Z. Zheng, G. Zheng, L. R. Giam, H. Zhang, C. A. Mirkin, Polymer pen lithography. *Science* **321**, 1658–1660 (2008).
30. A. J. Hart, A. H. Slocum, Rapid growth and flow-mediated nucleation of millimeter-scale aligned carbon nanotube structures from a thin-film catalyst. *J. Phys. Chem. B* **110**, 8250–8257 (2006).
31. S. Tawfick, X. Deng, A. J. Hart, J. Lahann, Nanocomposite microstructures with tunable mechanical and chemical properties. *Phys. Chem. Chem. Phys.* **12**, 4446–4451 (2010).
32. M. F. L. De Volder, S. J. Park, S. H. Tawfick, D. O. Vidaud, A. J. Hart, Fabrication and electrical integration of robust carbon nanotube micropillars by self-directed elastocapillary densification. *J. Micromech. Microeng.* **21**, 045033 (2011).
33. M. Bedewy, E. R. Meshot, M. J. Reinker, A. J. Hart, Population growth dynamics of carbon nanotubes. *ACS Nano* **5**, 8974–8989 (2011).
34. M. R. Maschmann, G. J. Ehlert, S. Tawfick, A. J. Hart, J. W. Baur, Continuum analysis of carbon nanotube array buckling enabled by anisotropic elastic measurements and modeling. *Carbon* **66**, 377–386 (2014).
35. P. D. Bradford, X. Wang, H. Zhao, Y. T. Zhu, Tuning the compressive mechanical properties of carbon nanotube foam. *Carbon* **49**, 2834–2841 (2011).
36. O. Yaglioglu, A. Cao, A. J. Hart, R. Martens, A. H. Slocum, Wide range control of microstructure and mechanical properties of carbon nanotube forests: A comparison between fixed and floating catalyst CVD techniques. *Adv. Funct. Mater.* **22**, 5028–5037 (2012).
37. M. Bedewy, E. R. Meshot, H. Guo, E. A. Verploegen, W. Lu, A. J. Hart, Collective mechanism for the evolution and self-termination of vertically aligned carbon nanotube growth. *J. Phys. Chem. C* **113**, 20576–20582 (2009).
38. E. R. Meshot, E. Verploegen, M. Bedewy, S. Tawfick, A. R. Woll, K. S. Green, M. Hromalik, L. J. Koerner, H. T. Philipp, M. W. Tate, S. M. Gruner, A. J. Hart, High-speed in situ x-ray scattering of carbon nanotube film nucleation and self-organization. *ACS Nano* **6**, 5091–5101 (2012).
39. W. C. Oliver, G. M. Pharr, Measurement of hardness and elastic modulus by instrumented indentation: Advances in understanding and refinements to methodology. *J. Mater. Res.* **19**, 3–20 (2004).
40. C. T. Wirth, S. Hofmann, J. Robertson, Surface properties of vertically aligned carbon nanotube arrays. *Diamond Relat. Mater.* **17**, 1518–1524 (2008).
41. C. Chen, B. Liang, A. Ogino, X. Wang, M. Nagatsu, Oxygen functionalization of multiwall carbon nanotubes by microwave-excited surface-wave plasma treatment. *J. Phys. Chem. C* **113**, 7659–7665 (2009).
42. S. Tawfick, Z. Zhao, M. Maschmann, A. Brieland-Shoultz, M. De Volder, J. W. Baur, W. Lu, A. J. Hart, Mechanics of capillary forming of aligned carbon nanotube assemblies. *Langmuir* **29**, 5190–5198 (2013).

43. M. De Volder, A. J. Hart, Engineering hierarchical nanostructures by elastocapillary self-assembly. *Angew. Chem. Intl. Ed.* **52**, 2412–2425 (2013).
44. M. De Volder, S. H. Tawfick, S. J. Park, D. Copic, Z. Zhao, W. Lu, A. J. Hart, Diverse 3D microarchitectures made by capillary forming of carbon nanotubes. *Adv. Mater.* **22**, 4384–4389 (2010).
45. M. Gupta, K. K. Gleason, Initiated chemical vapor deposition of poly(1H,1H,2H,2H-perfluorodecyl acrylate) thin films. *Langmuir* **22**, 10047–10052 (2006).
46. J. A. Rogers, Z. Bao, K. Baldwin, A. Dodabalapur, B. Crone, V. R. Raju, V. Kuck, H. Katz, K. Amundson, J. Ewing, P. Drzaic, Paper-like electronic displays: Large-area rubber-stamped plastic sheets of electronics and microencapsulated electrophoretic inks. *Proc. Natl. Acad. Sci. U.S.A.* **98**, 4835–4840 (2001).
47. H.-Y. Tseng, V. Subramanian, All inkjet-printed, fully self-aligned transistors for low-cost circuit applications. *Org. Electron.* **12**, 249–256 (2011).
48. A. Kamyshny, S. Magdassi, Conductive nanomaterials for printed electronics. *Small* **10**, 3515–3535 (2014).
49. J. Perelaer, R. Jani, M. Grouchko, A. Kamyshny, S. Magdassi, U. S. Schubert, Plasma and microwave flash sintering of a tailored silver nanoparticle ink, yielding 60% bulk conductivity on cost-effective polymer foils. *Adv. Mater.* **24**, 3993–3998 (2012).
50. D. S. Hecht, L. Hu, G. Irvin, Emerging transparent electrodes based on thin films of carbon nanotubes, graphene, and metallic nanostructures. *Adv. Mater.* **23**, 1482–1513 (2011).
51. K. Ellmer, Past achievements and future challenges in the development of optically transparent electrodes. *Nat. Photonics* **6**, 809–817 (2012).
52. J. Li, L. Hu, L. Wang, Y. Zhou, G. Grüner, T. J. Marks, Organic light-emitting diodes having carbon nanotube anodes. *Nano Lett.* **6**, 2472–2477 (2006).
53. S. Bae, H. Kim, Y. Lee, X. Xu, J.-S. Park, Y. Zheng, J. Balakreishnan, T. Lei, H. R. Kim, Y. I. Song, Y.-J. Kim, K. S. Kim, B. Özyilmaz, J.-H. Ahn, B. H. Hong, S. Iijima, Roll-to-roll production of 30-inch graphene films for transparent electrodes. *Nat. Nanotechnol.* **5**, 574–578 (2010).
54. D.-S. Leem, A. Edwards, M. Faist, J. Nelson, D. D. C. Bradley, J. C. de Mello, Efficient organic solar cells with solution-processed silver nanowire electrodes. *Adv. Mater.* **23**, 4371–4375 (2011).
55. T. M. Barnes, M. O. Reese, J. D. Bergeson, B. A. Larsen, J. L. Blackburn, M. C. Beard, J. Bult, J. van de Lagemaat, Comparing the fundamental physics and device performance of transparent, conductive nanostructured networks with conventional transparent conducting oxides. *Adv. Energy Mater.* **2**, 353–360 (2012).
56. W.-K. Kim, S. Lee, D. H. Lee, I. H. Park, J. S. Bae, T. W. Lee, J.-Y. Kim, J. H. Park, Y. C. Cho, C. R. Cho, S-Y. Jeong, Cu mesh for flexible transparent conductive electrodes. *Sci. Rep.* **5**, 10715 (2015).
57. B. D. Gates, Q. Xu, M. Stewart, D. Ryan, C. G. Willson, G. M. Whitesides, New approaches to nanofabrication: Molding, printing, and other techniques. *Chem. Rev.* **105**, 1171–1196 (2005).
58. T.-H. Kim, K.-S. Cho, E. K. Lee, S. J. Lee, J. Chae, J. W. Kim, D. H. Kim, J.-Y. Kwon, G. Amaratunga, S. Y. Lee, B. L. Choi, Y. Kuk, J. M. Kim, K. Kim, Full-colour quantum dot displays fabricated by transfer printing. *Nat. Photonics* **5**, 176–182 (2011).
59. A. Carson, A. M. Bowen, Y. Huang, R. G. Nuzzo, J. A. Rogers, Transfer printing techniques for materials assembly and micro/nanodevice fabrication. *Adv. Mater.* **24**, 5284–5318 (2012).
60. B. Basnar, I. Willner, Dip-pen-nanolithographic patterning of metallic, semiconductor, and metal oxide nanostructures on surfaces. *Small* **5**, 28–44 (2009).
61. S.-C. Hung, O. A. Nafday, J. R. Haaheim, F. Ren, G. C. Chi, S. J. Pearton, Dip pen nanolithography of conductive silver traces. *J. Phys. Chem. C* **114**, 9672–9677 (2010).
62. B. Y. Ahn, E. B. Duoss, M. J. Motala, X. Guo, S.-I. Park, Y. Xiong, J. Yoon, R. G. Nuzzo, J. A. Rogers, J. A. Lewis, Omnidirectional printing of flexible, stretchable, and spanning silver microelectrodes. *Science* **323**, 1590–1593 (2009).
63. B. Y. Ahn, D. J. Lorang, J. A. Lewis, Transparent conductive grids via direct writing of silver nanoparticle inks. *Nanoscale* **3**, 2700–2702 (2011).
64. M. S. Onses, E. Sutanto, P. M. Ferreira, A. G. Alleyne, J. A. Rogers, Mechanisms, capabilities, and applications of high-resolution electrohydrodynamic jet printing. *Small* **11**, 4237–4266 (2015).
65. M. Bedewy, B. Farmer, A. J. Hart, Synergetic chemical coupling controls the uniformity of carbon nanotube microstructure growth. *ACS Nano* **8**, 5799–5812 (2014).
66. D. N. Fubata, K. Hata, T. Yamada, T. Hiraoka, Y. Hayamizu, Y. Kakudate, O. Tanaike, H. Hatori, M. Yumura, S. Iijima, Shape-engineerable and highly densely packed single-walled carbon nanotubes and their application as super-capacitor electrodes. *Nat. Mater.* **5**, 987–994 (2006).
67. A. Perl, D. N. Reinhoudt, J. Huskens, Microcontact printing: Limitations and achievements. *Adv. Mater.* **21**, 2257–2268 (2009).
68. X. Zhou, H. Xu, J. Cheng, N. Zhao, S.-C. Chen, Flexure-based roll-to-roll platform: A practical solution for realizing large-area microcontact printing. *Sci. Rep.* **5**, 10402 (2015).
69. C. Y. Hui, A. Jagota, Y. Y. Lin, E. J. Kramer, Constraints on microcontact printing imposed by stamp deformation. *Langmuir* **18**, 1394–1407 (2002).
70. J. E. Petrzelka, D. E. Hardt, Static load-displacement behavior of PDMS microfeatures for soft lithography. *J. Micromech. Microeng.* **22**, 075015 (2012).
71. M. P. Down, L. Jiang, J. W. McBride, Investigating the benefits of a compliant gold coated multi-walled carbon nanotube contact surface in micro-electro mechanical systems switching. *Appl. Phys. Lett.* **107**, 071901 (2015).
72. A. Cao, P. L. Dickrell, W. G. Sawyer, M. N. Ghasemi-Nejhad, P. M. Ajayan, Super-compressible foamlike carbon nanotube films. *Science* **310**, 1307–1310 (2005).
73. J. Suhr, P. Victor, L. Ci, S. Sreekala, X. Zhang, O. Nalamasu, P. M. Ajayan, Fatigue resistance of aligned carbon nanotube arrays under cyclic compression. *Nat. Nanotechnol.* **2**, 417–421 (2007).
74. S. Pathak, E. J. Lim, P. P. S. S. Abadi, S. Graham, B. A. Cola, J. R. Greer, Higher recovery and better energy dissipation at faster strain rates in carbon nanotube bundles: An in-situ study. *ACS Nano* **6**, 2189–2197 (2012).
75. D. H. Lee, J. E. Kim, T. H. Han, J. W. Hwang, S. Jeon, S.-Y. Choi, S. H. Hong, W. J. Lee, R. S. Ruoff, S. O. Kim, Versatile carbon hybrid films composed of vertical carbon nanotubes grown on mechanically compliant graphene films. *Adv. Mater.* **22**, 1247–1252 (2010).
76. J. W. Elmer, O. Yaglioglu, R. D. Schaeffer, G. Kardos, O. Derkach, Direct patterning of vertically aligned carbon nanotube arrays to 20 μm pitch using focused laser beam micromachining. *Carbon* **50**, 4114–4122 (2012).
77. B. Rajabifar, S. Kim, K. Slinker, G. J. Ehlert, A. J. Hart, M. R. Maschmann, Three-dimensional machining of carbon nanotube forests using water-assisted scanning electron microscope processing. *Appl. Phys. Lett.* **107**, 143102 (2015).

Acknowledgments

Funding: Financial support to S.K. and A.J.H. was provided by the Massachusetts Institute of Technology (MIT) Department of Mechanical Engineering (startup funds to A.J.H.), the NSF (CMMI-1463181), and the Young Investigator Program of the Air Force Office of Scientific Research (FA9550-11-1-0089). Financial support to H.Z. was provided by the NIH (1R21HL114011-01A1). CNT catalyst deposition, patterning, and CNT plasma treatment were performed at the Microsystems Technology Laboratories at the MIT and the Center for Nanoscale Systems at the Harvard University. Nanoindentation was performed at the NanoMechanical Technology Laboratory at the MIT. Microscopy, spectrophotometry, and four-point probe measurements were performed at the MIT Center for Materials Science and Engineering. Fluorescence microscopy was performed at the Institute for Soldier Nanotechnologies at the MIT. **Author contributions:** A.J.H. and S.K. conceived the research idea and approach. A.J.H. supervised the project. S.K., H.S., K.K.G., and A.J.H. designed the stamp fabrication procedures. S.K., H.S., and H.Z. fabricated and characterized the stamps. D.M., S.K., and A.J.H designed the desktop P2R printing apparatus, and D.M. built the apparatus. S.K. and D.M. performed the printing experiments and characterization, and S.K. developed the contact model. S.K. and A.J.H. wrote the manuscript. All authors discussed the results and reviewed the manuscript. **Competing interests:** The authors declare that they have no competing interests. **Data and materials availability:** All data needed to evaluate the conclusions in the paper are present in the manuscript and/or the Supplementary Materials. Additional data related to this paper may be requested from the authors.

Submitted 19 July 2016
Accepted 4 November 2016
Published 7 December 2016
10.1126/sciadv.1601660

Citation: S. Kim, H. Sojoudi, H. Zhao, D. Mariappan, G. H. McKinley, K. K. Gleason, A. J. Hart, Ultrathin high-resolution flexographic printing using nanoporous stamps. *Sci. Adv.* **2**, e1601660 (2016).

Science Advances

Ultrathin high-resolution flexographic printing using nanoporous stamps

Sanha Kim, Hossein Sojoudi, Hangbo Zhao, Dhanushkodi Mariappan, Gareth H. McKinley, Karen K. Gleason and A. John Hart

Sci Adv **2** (12), e1601660.
DOI: 10.1126/sciadv.1601660